

## Article

# Microstructure and Tensile Property of Hybrid Fabricated Ti-6Al-4V Alloy by Investment Casting and Laser Additive Manufacturing

Xiao Zong<sup>1,2</sup>, Zhijun Ji<sup>1,2</sup>, Zijun Zhao<sup>1</sup>, Xin Feng<sup>1,2</sup>, Xianfei Ding<sup>1,2,\*</sup>  and Hai Nan<sup>1,2</sup><sup>1</sup> AECC Beijing Institute of Aeronautical Materials, Beijing 100095, China<sup>2</sup> Advanced Titanium Alloy Precision Forming Technology, Beijing 100094, China

\* Correspondence: xianfeimail@gmail.com; Tel.: +86-10-6249-8477

**Abstract:** Hybrid manufacturing of titanium alloys by investment casting and laser additive manufacturing (LAM) combines the advantages of both techniques and can further reduce the cost. In this study, microstructure evolution in the bonding zone and tensile property of the hybrid manufacturing Ti-6Al-4V alloy are carefully investigated. Results show that the hybrid sample consists of the LAM zone, the heat-affected zone (HAZ) and the base casting zone. A transition zone (TZ) forms within the HAZ close to the fusion line. Grains in the bottom of the LAM zone are much finer with a mixture of equiaxed grain and small columnar grain, and gradually coarsening to fully large columnar grains. Typical ultra-fine basket-wave microstructure forms in the LAM zone. In the TZ, the microstructure gradually changes from a fine basket-wave microstructure to a coarsened bimodal microstructure. The highest microhardness of the bonding zone is 491 HV. The fracture of the hybrid sample occurs in the casting half, and the tensile strength of the hybrid sample reaches  $(821 \pm 31)$  MPa, which is higher than that of the pure casting sample ( $(778 \pm 22)$  MPa). However, the elongation of the hybrid sample  $(8.0 \pm 0.5)\%$  is lower than that of the pure casting sample  $(10.0 \pm 1.7)\%$ .

**Keywords:** hybrid manufacturing; casting; laser additive manufacturing; titanium alloy; mechanical property



**Citation:** Zong, X.; Ji, Z.; Zhao, Z.; Feng, X.; Ding, X.; Nan, H. Microstructure and Tensile Property of Hybrid Fabricated Ti-6Al-4V Alloy by Investment Casting and Laser Additive Manufacturing. *Metals* **2023**, *13*, 668. <https://doi.org/10.3390/met13040668>

Academic Editor: Matteo Benedetti

Received: 16 February 2023

Revised: 3 March 2023

Accepted: 5 March 2023

Published: 28 March 2023



**Copyright:** © 2023 by the authors. Licensee MDPI, Basel, Switzerland. This article is an open access article distributed under the terms and conditions of the Creative Commons Attribution (CC BY) license (<https://creativecommons.org/licenses/by/4.0/>).

## 1. Introduction

Titanium alloys have excellent corrosion resistance, high temperature strength, low density, and biocompatibility. Thus, it is increasingly used for aerospace, biomedical, and chemical applications [1–3]. Investment casting is a well-established process for low-cost manufacturing of near-net-shape titanium alloy parts, especially for the mass production of large-size and intricate geometry components. However, the generation of shrinkage cavities, porosities and the slow solidification rate resulted coarse microstructures in casting titanium alloys usually lead to relatively poor mechanical properties [4]. Laser additive manufacturing (LAM) is also a method to build near-net-shape titanium alloy parts which fuse and consolidate metal powders layer by layer. It offers the advantages of tool-free, fully-dense production of complex geometries with dramatically reduced machining costs and materials waste. Moreover, owing to the rapid solidification resulted fine microstructures, LAM titanium alloys possess excellent mechanical properties comparable or even superior to the wrought materials [5,6]. Nevertheless, despite the variety of advantages, manufacturing costs and process time in LAM rise rapidly with part size, especially for mass production [7].

To use the advantages of both investment casting and LAM processes optimally, a hybrid production route is proposed by creating additive structures directly on a unitary investment casting component. For example, stamping dies have been rapidly manufactured based on the combination of digital patternless casting and high-power laser cladding for automotive panels [7,8]. In the hybrid route, simply shaped, large-volume

areas are investment-cast due to time and cost considerations, whereas functionalized, high-performance demand or highly complex component areas, for example stiffening structures and geometry-flexible joining elements, are produced additively. There is no doubt that the casting/LAM hybrid manufacturing technique can further increase the material utilization ratio and reduce the cost. It also has a great potential for the manufacturing of dual- or multi-functional titanium or titanium-based parts to realize the right materials utilized in the right positions [9].

One common concern of the casting/LAM hybrid manufacturing technique is the mechanical property of the final part, which is predominantly dependent on the microstructure of the bonding zone [10]. Research on laser welding or laser repairing titanium alloys generally suggested that the formation of the heat-affected zone deteriorated the mechanical properties of the whole samples [11–13]. However, Zhu et al. [14] reported that no grain growth was found in the HAZ of the wrought/LAM hybrid fabricated Ti–6.5Al–3.5Mo–1.5Zr–0.3Si titanium alloy, the tensile strength of the bonding zone was between the higher strength LAM sample and the lower strength wrought sample with the fracture position all found in the wrought sample side. Studies on the casting/LAM hybrid manufacturing TNM titanium aluminum alloy found that hardness in the bonding zone was highest owing to the microstructure variation [15]. Therefore, understanding the microstructure evolution mechanism and the mechanical properties of the casting/LAM hybrid manufacturing titanium alloy is of great significance for the engineering applications of this technology.

Ti-6Al-4V titanium alloy (TC4), as one of the most used titanium alloys in aerospace, has been well studied in investment casting [16–20] and LAM [17,21–25] techniques, respectively. However, there was a lack of relevant discussion about the casting/LAM hybrid manufacturing TC4 in previous research. In this study, microstructure and hardness variation in the bonding zone are characterized, microstructure evolution during the casting/LAM hybrid manufacturing process is carefully discussed, and the tensile properties of the hybrid manufacturing TC4 sample are investigated.

## 2. Materials and Experimental Procedures

TC4 substrate with the dimension of 150 mm × 150 mm × 20 mm was investment cast in a mould with yttria as the face coat material. The as-cast substrate was hot isostatically pressed (930 °C/130 MPa/2 h) and heat treated (730 °C/2 h, furnace cooling) to reduce cast defects and obtain well mechanical properties. The microstructure of the as-cast substrate exhibits typical coarse widmanstätten microstructure, and the width of the lamellar  $\alpha$  is about 3.6  $\mu\text{m}$ . The surface of the as-cast substrate was polished to a roughness of  $R_a \sim 0.6 \mu\text{m}$  and cleaned with acetone before the LAM process. Spherical powders of TC4 titanium alloy with particle sizes ranging from 75 to 150  $\mu\text{m}$  diameter were used for the LAM process. The LAM process was carried out in an LMD-V laser melting deposition additive manufacturing system equipped with a 3-kW fiber laser at room temperature. The oxygen content in the argon-purged laser melting deposition chamber was controlled below 30 ppm during the LAM process.

The detailed parameters of the LAM process were as follows: laser beam power 600 W, beam diameter 1 mm, scanning speed 700 mm/min, powder delivery rate (300–500) g/h, overlap ratio (30–50)%. The scanning path was a bidirectional mode (Figure 1a), meaning that the scanning directions of adjacent tracks were opposite. A thick plate of LAM TC4 titanium alloy with the dimension of 50 mm × 20 mm × 20 mm was fabricated (Figure 1b), and the hybrid sample was directly tempered at 580 °C for 2 h to relieve residual thermal stresses without changing the microstructure. The original surface of the as-cast substrate before the LAM process was defined as the nominal interface (yellow dot line in Figure 1a).

The plane parallel to the YZ plane was chosen for microstructure observation in the hybrid sample (Figure 1a). Metallographic specimens were prepared using the standard preparation method. A mixture solution of HF: HNO<sub>3</sub>:H<sub>2</sub>O with a ratio of 1:6:43 was used as the etching agent. The macro and microstructures of the specimens were examined by a digital camera, optical microscope (OM) and scanning electron microscope (SEM). The

microhardness was tested using a Vickers tester with a 300 g load and 15 s dwelling time. In each position, five indentations were conducted to guarantee the accuracy of data. The tensile specimens of the hybrid sample, with the nominal interface in the middle, were cut from the fabricated hybrid plate with a loading axis parallel to the building direction (Figure 1a), and the geometry of the tensile test specimen was illustrated in Figure 1c. The tensile specimens of pure casting samples were also prepared as references. Tensile testing was performed at room temperature in the air on Instron 5966 machine at a constant strain rate of  $10^{-3} \text{ s}^{-1}$  according to GB/T 228.1–2021, and a dynamic strain gauge extensometer was applied to record the strain. For each tensile test, three specimens were used to calculate the average values and standard deviations of strengths and elongations. The fracture surfaces were examined by SEM.

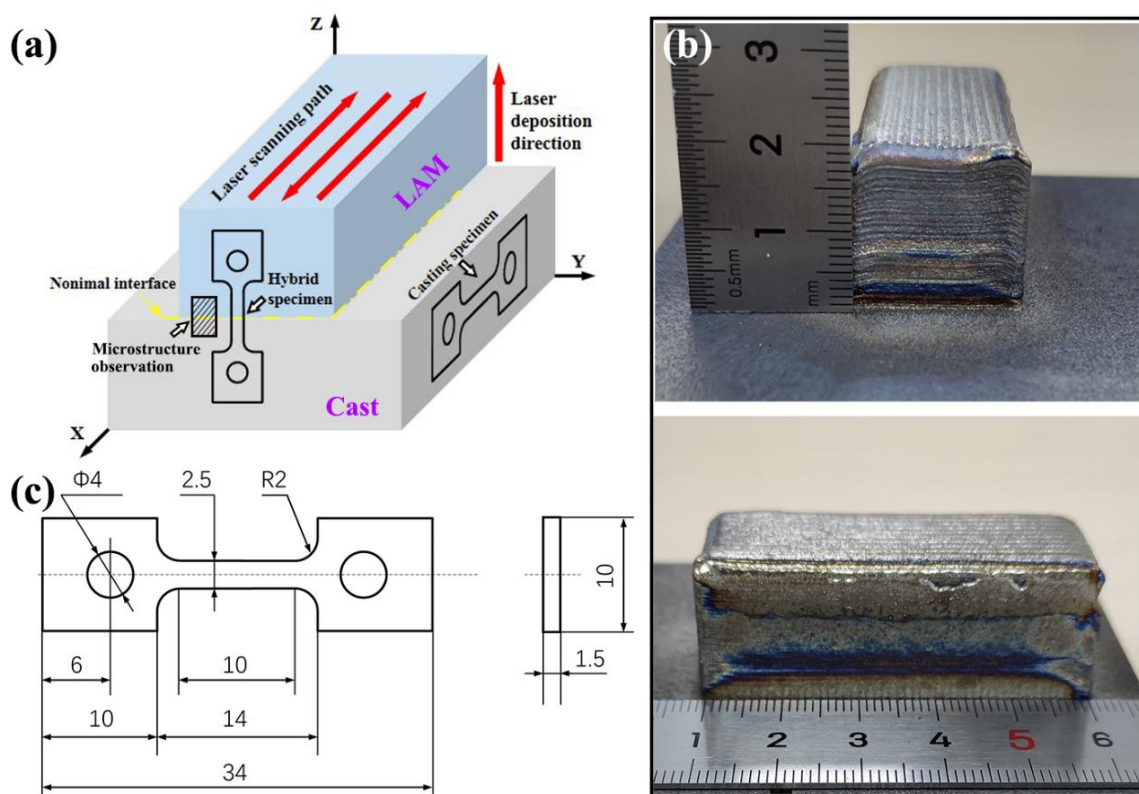


**Figure 1.** (a) Schematic illustration of the hybrid fabricating process and the sampling positions for microstructure observation and tensile test, (b) the hybrid manufactured TC4 sample, (c) schematic illustration of the tensile specimen.

### 3. Results

#### 3.1. Microstructure

Figure 2a presents the macrostructure of the hybrid TC4 sample, and no solidification defects are found. The interface between the first-laser deposition layer and the casting substrate is defined as the fusion line, which is located below the nominal interface. Owing to the different grain morphologies, three different zones can be clearly observed in the YZ plane of the hybrid sample: the laser additive manufacturing zone (LAM zone), the heat affected zone (HAZ) and the base casting zone. As can be seen in Figure 2a,b, different from the coarse equiaxed grain morphology in the base casting zone, the grain size in the bottom of the LAM zone is small and exhibits a mixed morphology of equiaxed grain and columnar grain.

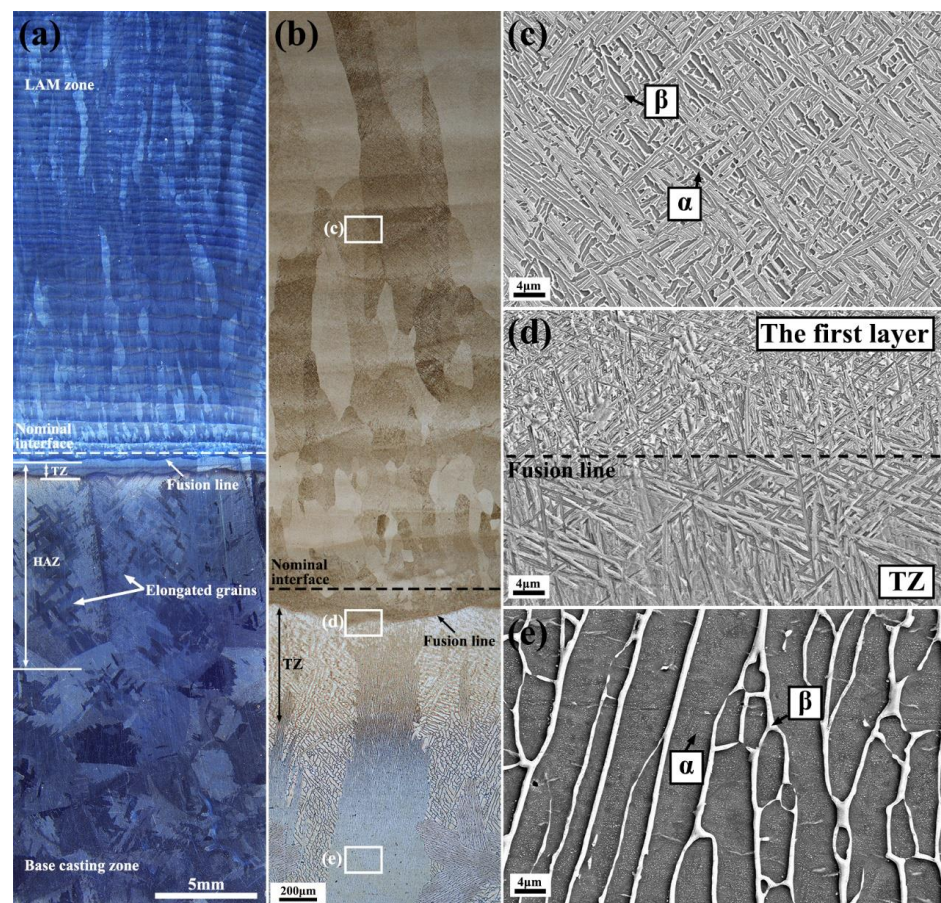


**Figure 2.** (a) Macrostructure of the hybrid sample in YZ plane, (b) OM image of the hybrid sample showing different regions, (c–e) corresponding higher magnification images in (b).

With the increment of the deposition layers, grains in the LAM zone gradually coarsen to fully large columnar grains, and the width of the columnar grain is stable at about (150~400)  $\mu\text{m}$  in the middle and upper regions of the LAM zone. Owing to the character of the intense epitaxial and large temperature gradient, the large columnar grains can grow consecutively through many layers [26,27]. In the HAZ, obvious grain growth can be found. Grains in the HAZ are elongated with columnar morphology due to the rapid heat dissipation of the substrate, whereas the average width and length of the elongated grain can reach about 4.8 mm and 9.2 mm, respectively. According to the grain morphologies in the hybrid sample, the region composed of the mixed grain zone in the LAM half and the HAZ in the casting half is defined as the bonding zone.

A transition zone (TZ) can be further found in the HAZ beneath the fusion line with the same contrast as the LAM zone. According to Figure 2b, the depth of the TZ is about 600~800  $\mu\text{m}$ . Figure 2c–e present the higher magnification images of the LAM zone around the fusion line and the elongated grain in the HAZ, respectively. In the middle and upper regions of the LAM zone (Figure 2c), typical ultra-fine basket-wave microstructure forms within the large columnar grain due to the high-temperature gradient and the rapid cooling rate, and the average width of the lamellar  $\alpha$  is about 0.5  $\mu\text{m}$ . Distinct microstructure differences can be observed above and below the fusion line (Figure 2d). In the first laser deposition layer (above the fusion line), the extremely fine basket-wave microstructure is found, and the average width of the lamellar  $\alpha$  is only 0.2  $\mu\text{m}$ . Formation of this extremely fine lamellar  $\alpha$  is attributed to the cold substrate, resulting in a higher cooling rate during the first layer deposition. In the top of the TZ (below the fusion line), the fine basket-wave microstructure is found, and the width of the lamellar  $\alpha$  in this region is similar to that of the ultra-fine microstructure observed in Figure 2c, whereas the length of the  $\alpha$  lath is

much larger than that in the LAM zone. The microstructure in the elongated grain of the HAZ is almost the same as that of the base casting zone except for the slightly coarsened lamellar  $\alpha$  phase (Figure 2e).

The microstructure in the TZ of the hybrid sample is observed in detail and presented in Figure 3, where Figure 3b is acquired at 100  $\mu\text{m}$  from the fusion line, and Figure 3b–f is obtained at 100  $\mu\text{m}$  intervals, respectively. Different from the fine basket-wave microstructure adjacent to the fusion line, the bimodal microstructure consists of primary  $\alpha$  ( $\alpha_p$ ) and superfine  $\beta$  transformed microstructure (lamellar secondary  $\alpha$  ( $\alpha_s$ ) and retained  $\beta$ ) is observed with the depth close to the base casting zone. The volume fraction of  $\alpha_p$  increases from the near LAM side to the near base casting side in the TZ, whereas the volume fraction of  $\beta$  transformed microstructure and the size of  $\alpha_s$  changes on the opposite. The microstructure in Figure 3f is almost the same as that of the base casting zone except for a few broken and coarsened  $\beta$  phases. Similar microstructure changes are also found in the HAZ of hybrid fabricated Ti–6.5Al–3.5Mo–1.5Zr–0.3Si alloy by laser additive manufacturing and forging [14].

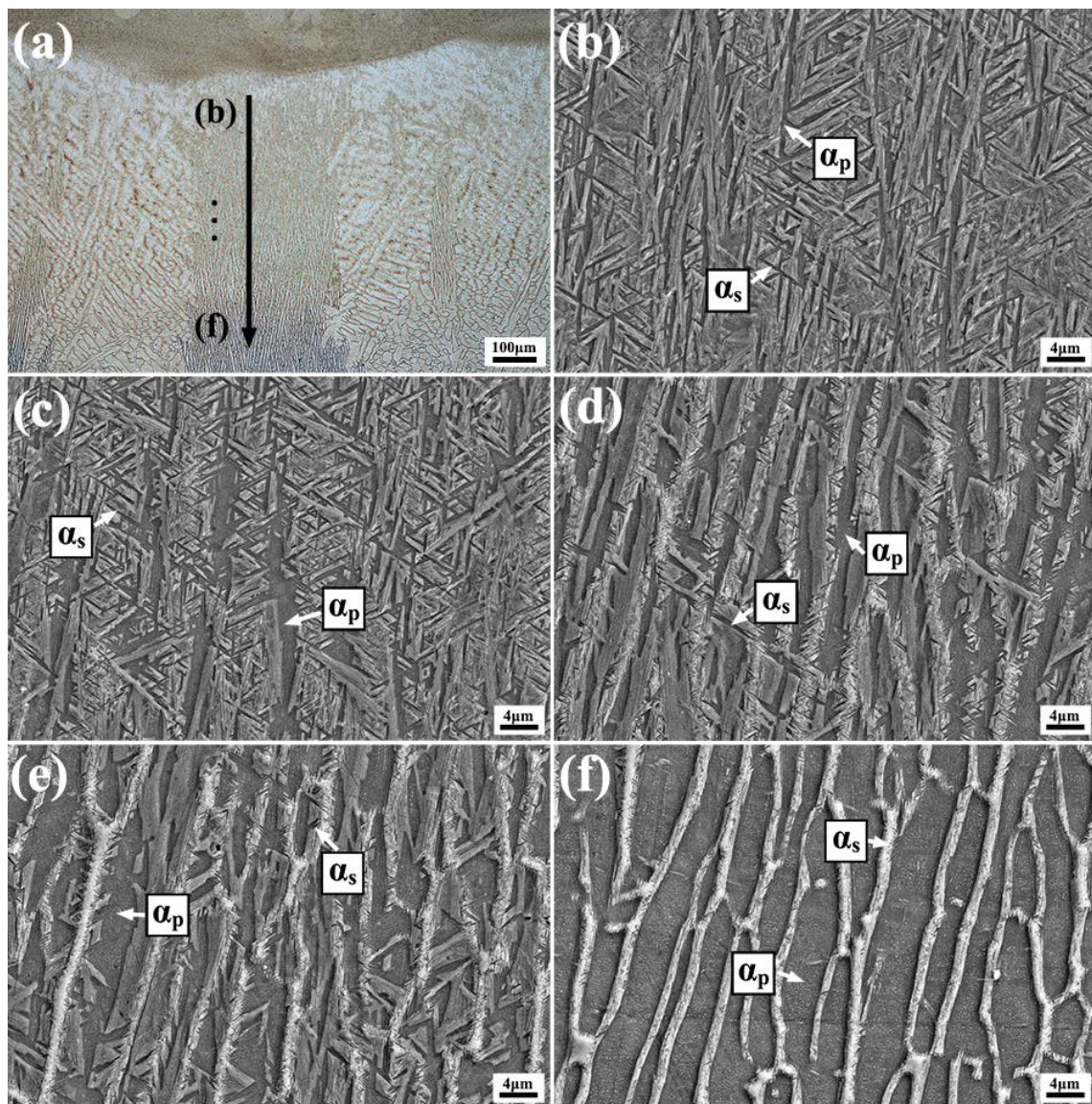


**Figure 3.** Microstructure in the TZ: (a) overview, (b–f) the corresponding higher magnification images in (a), obtained at 100  $\mu\text{m}$  intervals, respectively.

### 3.2. Hardness and Tensile Properties

The microhardness profile of the hybrid manufacturing TC4 sample is shown in Figure 4. The microhardness of the LAM zone in the upper large columnar grain region is about 420 HV, which is 105 HV higher than the base casting zone due to the refined microstructure. Taking the fusion line as the origin, microhardness in the range of  $-1000\ \mu\text{m}$ – $1400\ \mu\text{m}$  around the fusion line is measured in detail. The microstructure images corresponding to some of the typical locations are also presented in Figure 4. In general, microhardness in different locations of the hybrid sample is closely related to the  $\alpha$  lath morphology. As can be seen, microhardness in the extremely fine basket-wave microstructure region of the bonding zone is the highest ((b) in Figure 4). It reaches 491 HV. And then microhardness of the ultra-fine microstructure region ((a) in Figure 4), the fine microstructure region ((c) in Figure 4), the base casting zone ((f) in Figure 4) and the elongated grain region ((e) in Figure 4) reduces in order. In the HAZ, microhardness decreases as the distance from the fusion line increases due to the decrease in the  $\alpha_s$  phase and the coarsening of the  $\alpha$  or  $\alpha_p$  phase.

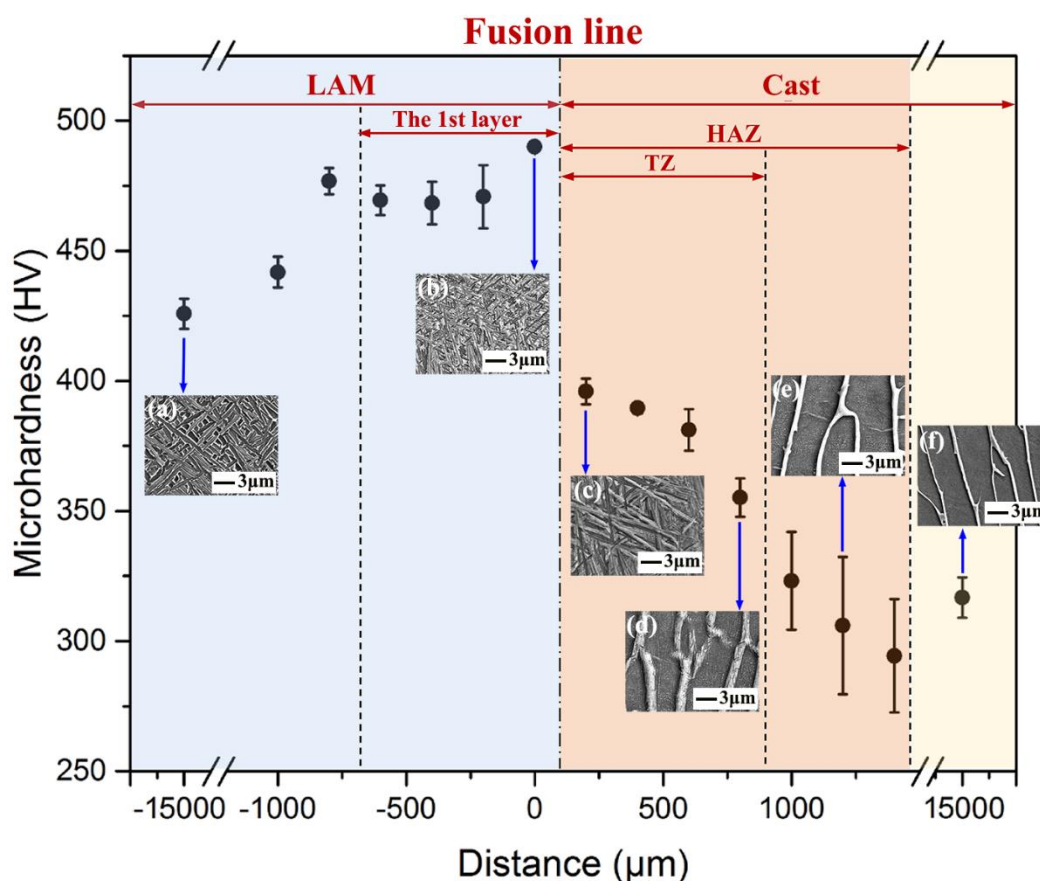


**Figure 4.** The microhardness profile of the hybrid manufacturing TC4 sample, in which the microstructure images correspond to some of the typical locations, is presented.

The room temperature tensile properties of the hybrid sample and the pure casting sample are shown in Table 1. The tensile property of the LAM sample is not tested in this research due to the size limitation and the anisotropy of the LAM sample. Instead, the tensile properties of the LAM TC4 alloy reported in other research [21–24] with similar microstructure characteristics as this research are listed in Table 1 as the reference. As can be seen, the strength of the hybrid sample falls between those of the LAM sample and the pure casting sample, whereas the elongation of the hybrid sample is the lowest among the three samples. Figure 5 presents the fracture position of the hybrid samples after the tensile test, and all the hybrid samples fracture at the HAZ of the casting half part. Fracture surfaces

of the pure casting sample and the hybrid sample are exhibited in Figure 6. The fracture surfaces of both samples consist of a fibrous zone and a shear rupture zone (Figure 6a,c). Higher magnification images (Figure 6b,d) show a dimpled morphology in the pure casting sample and mixed dimple and cleavage mode in the hybrid sample.

**Table 1.** Room temperature tensile properties of hybrid manufacturing TC4 sample, pure casting TC4 sample and LAM sample, data from [21–24].

Samples	$R_m$ , MPa	$R_{p0.2}$ , MPa	A, %
Hybrid	$821 \pm 31$	$775 \pm 24$	$8.0 \pm 0.5$
cast	$778 \pm 22$	$732 \pm 21$	$10.0 \pm 1.7$
LAM [21–24]	>950	>850	>9.0

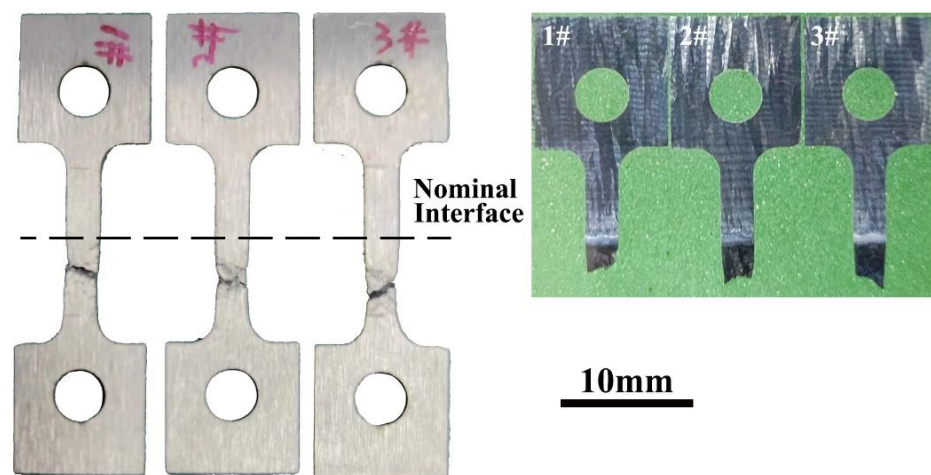


**Figure 5.** Hybrid samples after tensile test showing the fracture position.

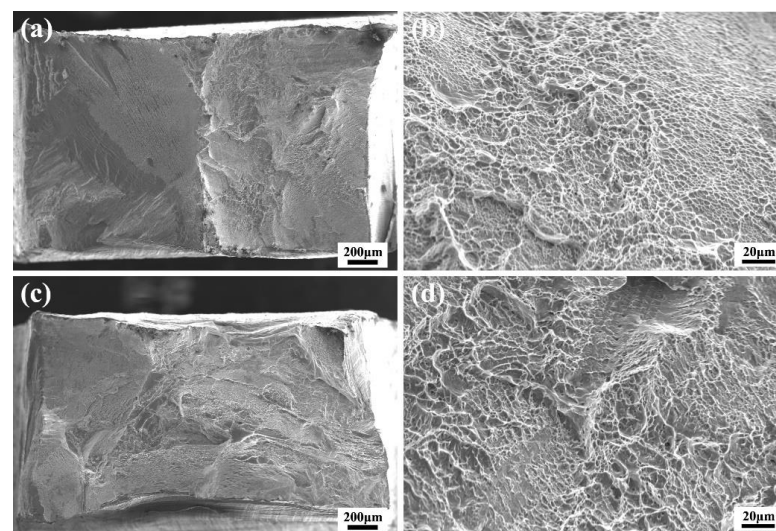


**Figure 6.** Fracture surfaces of the tensile specimens: (a) overview and (b) higher magnification image of the pure casting sample, (c) overview and (d) higher magnification image of the hybrid sample.

## 4. Discussion

### 4.1. Grain Morphology

According to Figure 2a,b, in this hybrid manufacturing process, grains in the bottom of the LAM zone are much finer with a mixture of equiaxed grain and small columnar

grain, and gradually coarsening to fully large columnar grains growing consecutively through many layers. A higher magnification image (Figure 7a) presents that the bottom small columnar grains are epitaxially grown from equiaxed grains and then competitive growth or are blocked by the equiaxed grains at the top of the deposition layer. Accordingly, Figure 7b schematically illustrates the grain formation mechanism at the bottom of the LAM zone. In the first layer of laser deposition, typical epitaxial growth of the parent casting grains occurs at the pool bottom, and equiaxed grains are formed at the top of the deposited layer. There are two mechanisms for the formation of equiaxed grains, the heterogeneous nucleation of the residual or partially melted solid powders and the columnar-to-equiaxed transition (CET) [28–31]. In the second layer of laser deposition, only part of the equiaxed grains is remelted, and the epitaxial growth of the preserved equiaxed grains occurs, forming small columnar grains. Within the melting pool, columnar grains grow competitively or are blocked by the equiaxed grains at the top of the deposition layer, forming a mixture of equiaxed grains and small columnar grains at the bottom of the LAM zone.

According to Figure 2c,d, the difference in the width of the lamellar  $\alpha$  between the bottom and upper regions of the LAM zone indicates the different cooling conditions of the melting pool at different heights of the LAM zone. During the first few layers of laser deposition, the temperature of the substrate/as-deposited part is relatively low. However, with the increment of the deposition layers, the heat accumulation in the as-deposited LAM zone increases the building temperature of the following deposition layer. Thus, it may lead to an increase in the depth of the melting pool [32]. Research on the melt depths developed by overlapped laser tracks on a Ti-6Al-4V alloy also suggested that the previous laser tracks may have a significant effect on the specimen temperature, resulting in a temperature that is different from the initial value and, in turn, makes an important contribution to the depth of the following laser tracks [33]. Therefore, in the middle and upper regions of the LAM zone, a larger remelting depth to the underlying deposited layer leads to the efficient elimination of the superficial equiaxed grains, and a fully large columnar grain structure is produced.

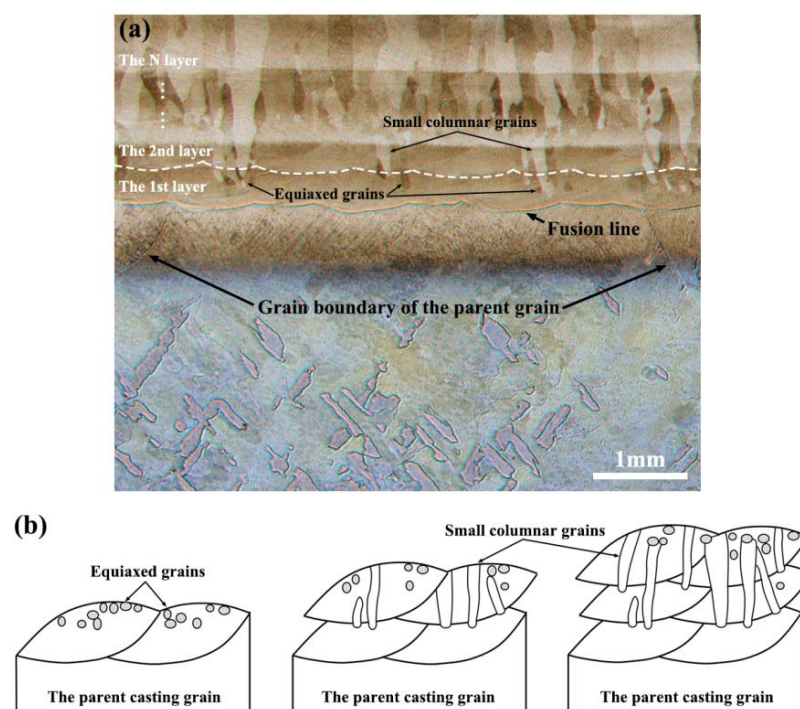


**Figure 7.** (a) Grains formed in the bonding zone of the hybrid sample, (b) schematic diagram illustrating the grain formation mechanism in the bottom of the LAM zone.

#### 4.2. Microstructure Evolution in the TZ

Microstructure evolution in the TZ of the hybrid sample during the LAM process can be schematically illustrated in Figure 8. When high-energy laser beam scans on the casting substrate, a high temperature melting pool forms and its beneath substrate is heated instantaneously, causing the formation of HAZ [34]. In the region adjacent to the melting pool, the peak temperature is inevitably above the  $\beta$  transus point ( $T_\beta$ ) of titanium alloy. As it approaches the core of the casting substrate, the peak temperature decreases gradually to  $T_{\alpha+\beta}$  and then to room temperature.  $T_\beta$  and  $T_{\alpha+\beta}$  region in the HAZ of the hybrid sample is schematically illustrated and separated by the white dotted line in Figure 8.

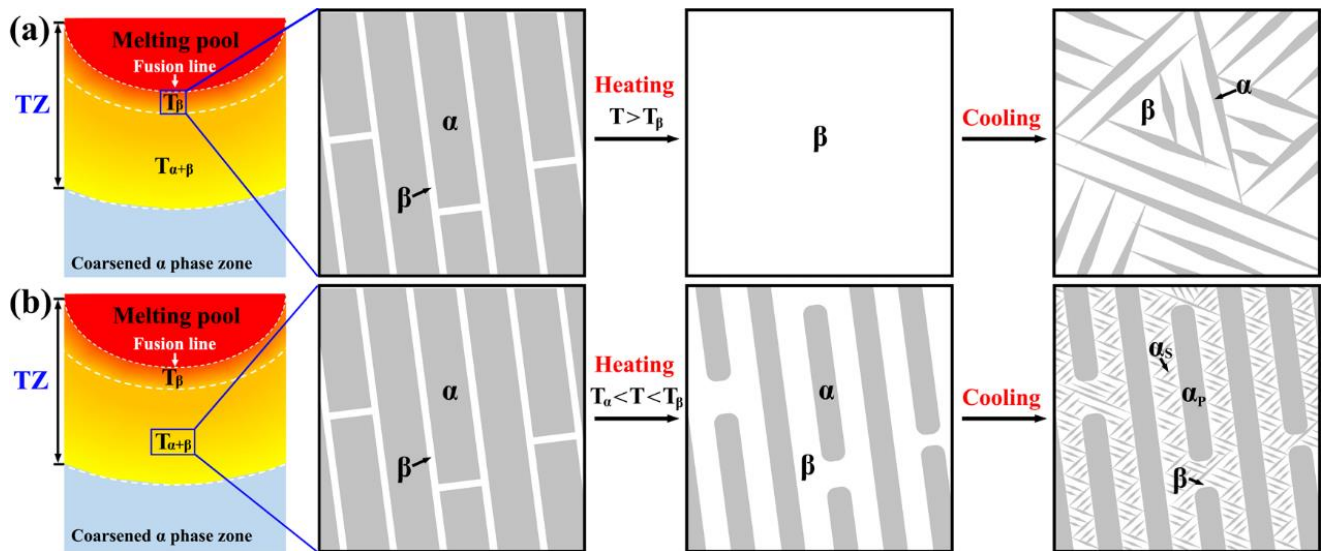


**Figure 8.** Schematic diagrams illustrate the microstructure evolution in the region (a) close to the fusion line, (b) close to the base casting zone of the TZ during the LAM process.

In the region adjacent to the melting pool ( $T_\beta$  region, Figure 8a), a completely  $\beta$  phase forms during laser heating. Then fine basket-wave microstructure can be formed during the subsequent rapid cooling. While in the  $T_{\alpha+\beta}$  region (Figure 8b), the widmanstätten casting microstructure transforms to a mixture of  $\beta$  phase and retained  $\alpha$  ( $\alpha_p$ ) under laser heating. The closer to the melting pool, the higher the peak temperature and the lower the content of primary  $\alpha$ . During the subsequent rapid cooling process,  $\beta \rightarrow \alpha$  allotropic transformation occurs, and secondary  $\alpha$  phase ( $\alpha_s$ ) precipitates. The bimodal microstructure consists of primary  $\alpha$  ( $\alpha_p$ ), and superfine  $\beta$  transformed microstructure (lamellar secondary  $\alpha$  ( $\alpha_s$ ) and retained  $\beta$ ) is thus formed in the  $T_{\alpha+\beta}$  region of the TZ (Figure 3). In the region far from the melting pool, the temperature drops to a certain degree that has little effect on the casting substrate, and the coarse widmanstätten microstructure remains.

#### 4.3. Fracture Mechanism

According to Table 1 and Figure 5, the tensile strength of the hybrid sample is higher than that of the pure casting sample, but its elongation is lower. The increased strength of the hybrid sample is mainly attributed to the smaller grain size and finer microstructure formed in the bonding zone. As revealed in Figure 9, the hybrid sample has refined grain and microstructure in one part and coarser in the other, whereas the pure casting sample has only coarse microstructure, which leads to the average grain size of the hybrid sample being smaller than that of the pure casting sample along the direction of maximum tensile stress, thus result in the increased strength of the hybrid sample (Hall-Petch effect). Moreover, the finer microstructure in the bonding zone (Figures 2d and 3) also contributes to the increased strength of the hybrid sample because the mean free path of dislocation is smaller in the fine microstructure region during the tensile deformation process (Figure 9).

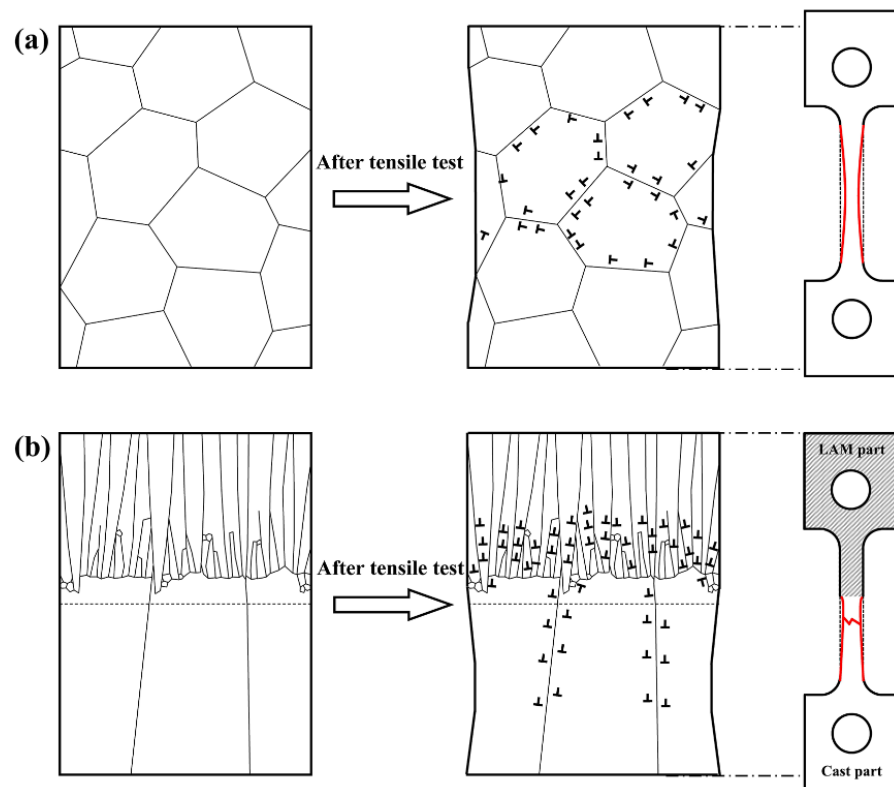


**Figure 9.** Schematic diagrams illustrate the fracture mechanism of (a) the pure casting sample and (b) the hybrid sample.

The decreased elongation of the hybrid sample is mainly due to the non-uniform deformation during the tensile process. Generally, plastic deformation occurs when tensile stress exceeds the yield strength of the alloy during the tensile process [35]. According to Table 1, the yield strength of the hybrid sample ( $(775 \pm 24)$  MPa) is a little higher than that of the pure casting sample ( $(732 \pm 21)$  MPa), both of which are much lower than that of the LAM sample ( $>950$  MPa). The ultimate tensile strengths of the hybrid sample and the pure casting sample are even lower than the yield strength of the LAM sample. During the tensile deformation of the hybrid sample, when the tensile stress increases to the yield strength of the hybrid sample, the casting half begins to yield, and obvious plastic deformation occurs. However, no obvious deformation occurs in the LAM half at the same time, because the tensile stress has not reached its yield strength. Until the tensile stress reaches the ultimate tensile strength of the hybrid sample and fracture happens in the HAZ of the casting half, the LAM half may still not experience obvious plastic deformation (Figure 9). Therefore, the casting half part contributes most of the total elongation of the hybrid sample, which is inevitably less than that obtained by the total length tensile pure casting sample. Similar phenomena are found in the tensile tests of forging/LAM hybrid-manufactured titanium alloys [14,36].

## 5. Conclusions

In this study, Ti-6Al-4V alloy is hybrid-fabricated by investment casting and laser additive manufacturing. Microstructure evolution in the bonding zone and tensile property of the hybrid sample are carefully investigated. The main findings can be summarized as follows:

- (1) The hybrid sample consists of the laser additive manufacturing zone, the heat-affected zone and the base casting zone. Within the heat-affected zone, phase transformation occurs in the region close to the fusion line, forming a transition zone.

- (2) Grains in the bottom of the LAM zone exhibit a mixture of equiaxed grain and small columnar grain and gradually coarsen to fully large columnar morphology growing consecutively through many layers in the middle and upper region. The width of the large columnar grain is stable at about (150~400)  $\mu\text{m}$ . While grains in the HAZ are elongated and exhibit columnar morphology. The average width and length of the elongated grain reach about 4.8 mm and 9.2 mm, respectively.
- (3) Ultra-fine basket-wave microstructure forms within the large columnar grain of the LAM zone, and extremely fine basket-wave microstructure forms just above the fusion line in the bonding zone. As the distance from the fusion line increases, the microstructure in the TZ transforms from a fine basket-wave microstructure to a bimodal microstructure.
- (4) Microhardness of the hybrid sample in the extremely fine basket-wave microstructure region of the bonding zone is the highest. It reaches 491 HV. Fracture of all the hybrid samples occurs in the HAZ of the casting half in tensile testing, and the tensile strength of the hybrid sample reaches  $(821 \pm 31)$  MPa, which is higher than that of the pure casting sample. While the elongation of the hybrid sample is lower than that of the pure casting sample.

**Author Contributions:** X.Z. and Z.J. conceived the idea. X.Z., Z.J. and Z.Z. designed the experiments and fabricated the samples. X.Z. and X.F. characterized the microstructures and properties. X.Z., Z.J. and X.D. analyzed the data and drafted the manuscript. X.D. and H.N. reconfirmed the microstructure and mechanical properties. H.N. supervised the work. All authors have read and agreed to the published version of the manuscript.

**Funding:** This research was funded by Beijing Natural Science Foundation (No. 2222092), National Science and Technology Major Project (No. J2019-VI-0003-0116) and National Key Research and Development Program (No. 2020YFB2008300).

**Data Availability Statement:** The datasets used or analyzed during the current study are available from the corresponding author upon reasonable request.

**Conflicts of Interest:** The authors declare that they have no known competing financial interests or personal relationships that could have appeared to influence the work reported in this paper.

## References

1. Attar, H.; Ehtemam-Haghighi, S.; Kent, D.; Wu, X.; Dargusch, M.S. Comparative study of commercially pure titanium produced by laser engineered net shaping, selective laser melting and casting processes. *Mater. Sci. Eng. A* **2017**, *705*, 385–393. [[CrossRef](#)]
2. Gangwar, K.; Ramulu, M. Friction stir welding of titanium alloys: A review. *Mater. Des.* **2018**, *141*, 230–255. [[CrossRef](#)]
3. Sun, Z.; Zhu, L.; Mo, X.; Nan, H.; Ding, X. Microstructure Characterization and Properties of Graphene Oxide-Reinforced TiAl Matrix Composites. *Metals* **2021**, *11*, 883. [[CrossRef](#)]
4. Shah, M.; Patel, D.R.; Pande, S. Additive manufacturing integrated Casting—A review. *Mater. Today Proc.* **2022**, *62*, 7199–7203. [[CrossRef](#)]
5. Tan, C.; Weng, F.; Sui, S.; Chew, Y.; Bi, G. Progress and perspectives in laser additive manufacturing of key aeroengine materials. *Int. J. Mach. Tools Manuf.* **2021**, *170*, 103804. [[CrossRef](#)]
6. Liu, G.; Chen, X.; He, X.; Cheng, Y.; Huo, L.; Yin, M.; Hao, J.; Chen, F.; Wang, S.; Yi, P.; et al. Additive manufacturing of structural materials. *Mater. Sci. Eng.* **2021**, *145*, 100596. [[CrossRef](#)]
7. Shan, Z.; Sun, F.; Liu, Y. Hybrid forming mechanism of patternless casting and laser cladding. *Front. Mech. Eng.* **2019**, *14*, 393–401. [[CrossRef](#)]
8. Polenz, S.; Oettel, M.; López, E.; Leyens, C. Hybrid Process Chain from Die Casting and Additive Manufacturing. *Light. Des. Worldw.* **2019**, *12*, 44–49. [[CrossRef](#)]
9. Gu, D.; Shi, X.; Poprawe, R.; Bourell, D.L.; Setchi, R.; Zhu, J. Material-structure-performance integrated laser-metal additive manufacturing. *Science* **2021**, *372*, 932. [[CrossRef](#)]
10. Xie, J.; Chen, Y.; Yin, L.; Zhang, T.; Wang, S.; Wang, L. Microstructure and mechanical properties of ultrasonic spot welding TiNi/Ti6Al4V dissimilar materials using pure Al coating. *J. Manuf. Process.* **2021**, *64*, 473–480. [[CrossRef](#)]
11. Chamanfar, A.; Huang, M.-F.; Pasang, T.; Tsukamoto, M.; Misiolek, W. Microstructure and mechanical properties of laser welded Ti-10V-2Fe-3Al (Ti1023) titanium alloy. *J. Mater. Res. Technol.* **2020**, *9*, 7721–7731. [[CrossRef](#)]
12. Zhao, Z.; Chen, J.; Zhang, Q.; Tan, H.; Lin, X.; Huang, W.-D. Microstructure and mechanical properties of laser additive repaired Ti17 titanium alloy. *Trans. Nonferrous Met. Soc. China* **2017**, *27*, 2613–2621. [[CrossRef](#)]

13. Yuhua, C.; Yuqing, M.; Weiwei, L.; Peng, H. Investigation of welding crack in micro laser welded NiTiNb shape memory alloy and Ti6Al4V alloy dissimilar metals joints. *Opt. Laser Technol.* **2017**, *91*, 197–202. [[CrossRef](#)]
14. Zhu, Y.; Li, J.; Tian, X.; Wang, H.; Liu, D. Microstructure and mechanical properties of hybrid fabricated Ti–6.5Al–3.5Mo–1.5Zr–0.3Si titanium alloy by laser additive manufacturing. *Mater. Sci. Eng. A* **2014**, *607*, 427–434. [[CrossRef](#)]
15. Rittinghaus, S.-K.; Schmelzer, J.; Rackel, M.; Hemes, S.; Vogelpoth, A.; Hecht, U.; Weisheit, A. Direct Energy Deposition of TiAl for Hybrid Manufacturing and Repair of Turbine Blades. *Materials* **2020**, *13*, 4392. [[CrossRef](#)]
16. Liu, J.; Zhang, K.; Yang, Y.; Wang, H.; Zhu, Y.; Huang, A. Grain boundary  $\alpha$ -phase precipitation and coarsening: Comparing laser powder bed fusion with as-cast Ti-6Al-4V. *Scr. Mater.* **2022**, *207*, 114261. [[CrossRef](#)]
17. Pessard, E.; Lavialle, M.; Laheurte, P.; Didier, P.; Brochu, M. High-cycle fatigue behavior of a laser powder bed fusion additive manufactured Ti-6Al-4V titanium: Effect of pores and tested volume size. *Int. J. Fatigue* **2021**, *149*, 106206. [[CrossRef](#)]
18. Boonchuduang, T.; Bootchanont, A.; Klysubun, W.; Amonpattaratkit, P.; Khamkongkao, A.; Puncreobutr, C.; Yimnirun, R.; Lohwongwatana, B. Formation of Alpha-Case Layer During Investment Casting of Pure Ti and Ti-6Al-4V Using Comparative XRD and EXAFS Investigation. *Met. Mater. Trans. A* **2019**, *51*, 586–596. [[CrossRef](#)]
19. Wu, G.; Cheng, X.; Sha, W.; Cheng, X.; Zhao, J.; Nan, H. Effect of the interaction layer on the mechanical properties of Ti–6Al–4V alloy castings. *Mater. Chem. Phys.* **2016**, *175*, 125–130. [[CrossRef](#)]
20. Feng, X.; Qiu, J.; Ma, Y.; Lei, J.; Cui, Y.; Wu, X.; Yang, R. Influence of Processing Conditions on Microstructure and Mechanical Properties of Large Thin-Wall Centrifugal Ti–6Al–4V Casting. *J. Mater. Sci. Technol.* **2016**, *32*, 362–371. [[CrossRef](#)]
21. Azarniya, A.; Colera, X.; Mirzaali, M.; Sovizi, S.; Bartolomeu, F.; Weglowski, M.S.; Wits, W.; Yap, C.; Ahn, J.; Miranda, G.; et al. Additive manufacturing of Ti–6Al–4V parts through laser metal deposition (LMD): Process, microstructure, and mechanical properties. *J. Alloys Compd.* **2019**, *804*, 163–191. [[CrossRef](#)]
22. Keist, J.S.; Palmer, T.A. Role of geometry on properties of additively manufactured Ti-6Al-4V structures fabricated using laser based directed energy deposition. *Mater. Des.* **2016**, *106*, 482–494. [[CrossRef](#)]
23. Carroll, B.E.; Palmer, T.A.; Beese, A.M. Anisotropic tensile behavior of Ti–6Al–4V components fabricated with directed energy deposition additive manufacturing. *Acta Mater.* **2015**, *87*, 309–320. [[CrossRef](#)]
24. Beese, A.M.; Carroll, B.E. Review of Mechanical Properties of Ti-6Al-4V Made by Laser-Based Additive Manufacturing Using Powder Feedstock. *JOM* **2015**, *68*, 724–734. [[CrossRef](#)]
25. Baufeld, B.; Brandl, E.; Van der Biest, O. Wire based additive layer manufacturing: Comparison of microstructure and mechanical properties of Ti–6Al–4V components fabricated by laser-beam deposition and shaped metal deposition. *J. Mater. Process. Technol.* **2011**, *211*, 1146–1158. [[CrossRef](#)]
26. Zong, X.; Li, Z.; Li, J.; Cheng, X.; Chen, R.; Tan, C.-W.; Wang, H.-M. High strain rate response of Ti-6.5Al-3.5Mo-1.5Zr-0.3Si titanium alloy fabricated by laser additive manufacturing. *J. Alloys Compd.* **2019**, *781*, 47–55. [[CrossRef](#)]
27. Jiao, Z.; Fu, J.; Li, Z.; Cheng, X.; Tang, H.; Wang, H. The spatial distribution of  $\alpha$  phase in laser melting deposition additive manufactured Ti-10V-2Fe-3Al alloy. *Mater. Des.* **2018**, *154*, 108–116. [[CrossRef](#)]
28. Zhang, G.; Lu, X.; Li, J.; Chen, J.; Lin, X.; Wang, M.; Tan, H.; Huang, W. In-situ grain structure control in directed energy deposition of Ti6Al4V. *Addit. Manuf.* **2022**, *55*, 102865. [[CrossRef](#)]
29. Ren, Y.; Lin, X.; Fu, X.; Tan, H.; Chen, J.; Huang, W. Microstructure and deformation behavior of Ti-6Al-4V alloy by high-power laser solid forming. *Acta Mater.* **2017**, *132*, 82–95. [[CrossRef](#)]
30. Riedlbauer, D.; Scharowsky, T.; Singer, R.F.; Steinmann, P.; Körner, C.; Mergheim, J. Macroscopic simulation and experimental measurement of melt pool characteristics in selective electron beam melting of Ti-6Al-4V. *Int. J. Adv. Manuf. Technol.* **2016**, *88*, 1309–1317. [[CrossRef](#)]
31. Zhu, Y.-Y.; Tang, H.-B.; Li, Z.; Xu, C.; He, B. Solidification behavior and grain morphology of laser additive manufacturing titanium alloys. *J. Alloys Compd.* **2019**, *777*, 712–716. [[CrossRef](#)]
32. Jeon, I.; Sohn, H. Online melt pool depth estimation in laser metal deposition using a coaxial thermography system. *J. Laser Appl.* **2022**, *34*, 022001. [[CrossRef](#)]
33. Hu, T.N.B.C. A semi-empirical model to predict the melt depth developed in overlapping laser tracks on a Ti-6Al-4V alloy. *J. Mater. Process. Technol.* **1999**, *94*, 116–122. [[CrossRef](#)]
34. Liang, L.; Xu, M.; Chen, Y.; Zhang, T.; Tong, W.; Liu, H.; Wang, H.; Li, H. Effect of welding thermal treatment on the microstructure and mechanical properties of nickel-based superalloy fabricated by selective laser melting. *Mater. Sci. Eng. A* **2021**, *819*, 141507. [[CrossRef](#)]
35. Liang, Y.-J.; Liu, D.; Wang, H.-M. Microstructure and mechanical behavior of commercial purity Ti/Ti–6Al–2Zr–1Mo–1V structurally graded material fabricated by laser additive manufacturing. *Scr. Mater.* **2014**, *74*, 80–83. [[CrossRef](#)]
36. Ma, J.; Zhang, Y.; Li, J.; Cui, D.; Wang, Z.; Wang, J. Microstructure and mechanical properties of forging-additive hybrid manufactured Ti–6Al–4V alloys. *Mater. Sci. Eng. A* **2021**, *811*, 140984. [[CrossRef](#)]

**Disclaimer/Publisher’s Note:** The statements, opinions and data contained in all publications are solely those of the individual author(s) and contributor(s) and not of MDPI and/or the editor(s). MDPI and/or the editor(s) disclaim responsibility for any injury to people or property resulting from any ideas, methods, instructions or products referred to in the content.